Searching for Subsurface Oceans on the Moons of Uranus Using Magnetic Induction

Benjamin P Weiss[1], John B. Biersteker[1], Vittorio Colicci[1], Allison Goode[1], Julie C Castillo-Rogez[2], Anastassios E. E Petropoulos[2], and Tibor S. Balint[2]

[1]Massachusetts Institute of Technology
[2]Jet Propulsion Laboratory

November 21, 2022

Abstract

Icy moons around the ice giant planets may contain subsurface oceans. Their oceans could be detected and characterized using measurements of magnetic fields induced by the host planet's time-varying magnetospheric field. We explore the possibility of detecting and characterizing subsurface oceans among the five major moons of Uranus—with a particular focus on Ariel—using spacecraft magnetometry measurements. We find that the magnetic field at each moon is dominated by the synodic frequency with amplitudes ranging from ˜4 nT at Oberon up to ˜300 nT at Miranda. If these bodies contain oceans with sufficient thicknesses (>˜6-100 km) and conductivities (>2 S m^{-1}), the induced surface fields should have amplitudes exceeding the typical ˜1 nT sensitivity of spacecraft magnetometry investigations. Furthermore, the magnetic field at the moons spans periods ranging from 1 to 10^3 h. This could enable long-term measurements to separately constrain ocean and ice thicknesses and ocean salinity.

Searching for Subsurface Oceans on the Moons of Uranus Using Magnetic Induction

Benjamin P. Weiss[1], John B. Biersteker[1], Vittorio Colicci[1], Allison Goode[1], Julie C. Castillo-Rogez[2], Anastassios E. Petropoulos[2], and Tibor S. Balint[2]

[1]Department of Earth, Atmospheric and Planetary Sciences, Massachusetts Institute of Technology, Cambridge MA, USA

[2]Jet Propulsion Laboratory, California Institute of Technology, Pasadena, CA, USA

Corresponding author: Benjamin Weiss (bpweiss@mit.edu)

Key Points:

- The surfaces of the Uranian moons show evidence for resurfacing following formation and therefore may contain subsurface oceans.
- Uranus's magnetic field may induce time-varying currents in these oceans that generate induced magnetic fields.
- Spacecraft measurements of such induced fields could detect oceans on each of the five major moons, especially Miranda and Ariel.

Keywords:

Uranus, ice giants, spacecraft missions, icy moons, magnetic induction, magnetometry

Abstract

Icy moons around the ice giant planets may contain subsurface oceans. Their oceans could be detected and characterized using measurements of magnetic fields induced by the host planet's time-varying magnetospheric field. We explore the possibility of detecting and characterizing subsurface oceans among the five major moons of Uranus—with a particular focus on Ariel—using spacecraft magnetometry measurements. We find that the magnetic field at each moon is dominated by the synodic frequency with amplitudes ranging from ~4 nT at Oberon up to ~300 nT at Miranda. If these bodies contain oceans with sufficient thicknesses (>~6-100 km) and conductivities (>2 S m^{-1}), the induced surface fields should have amplitudes exceeding the typical ~1 nT sensitivity of spacecraft magnetometry investigations. Furthermore, the magnetic field at the moons spans periods ranging from 1 to 10^3 h. This could enable long-term measurements to separately constrain ocean and ice thicknesses and ocean salinity.

Plain Language Summary

The icy moons of Uranus may harbor subsurface oceans. These oceans may be habitable environments and tell us about the moon's formation and evolution of their orbits. Here we explore the possibility that these oceans could be detected and characterized by magnetic field measurements from a spacecraft. In particular, the time-varying magnetic field of Uranus may generate currents in a salty ocean by the process of induction. These currents could then generate a secondary magnetic field detectable by a spacecraft flyby. Here we explore this possibility by calculating the ambient and induced magnetic fields around the five largest moons of Uranus: Miranda, Ariel, Umbriel, Titania, and Oberon. We find that the spin of Uranus and the orbital motion of the moons leads to strong time-varying fields at each moon. If these moons harbor thick (>10 km) oceans with salinities like that of Earth's oceans, their induced fields would likely be detectable by a close flyby. Longer term field measurements from a Uranus and/or dedicated icy moon orbiter could likely constrain the ocean and ice thickness and ocean salinity.

1 Introduction

Ocean worlds, planetary bodies with large-scale liquid water layers (Nimmo & Pappalardo, 2016), have been discovered amongst the icy moons of Jupiter and Saturn and perhaps beyond. Ocean worlds are of great interest for several reasons. Most importantly, they may be some of the most common potentially habitable environments in the solar system. Second, their volatile-rich interiors represent a unique end member of planetary structure. Third, they are natural laboratories for studying tides and the moons' coupled orbital and thermal evolution.

The icy moons of the ice giants are likely to be major targets of upcoming spacecraft missions [e.g., Balint et al. (2020); Elder et al. (2021); Hofstdater & Simon (2017)]. Here we explore the possibility of detecting and characterizing subsurface oceans on the five major moons of Uranus—Miranda, Ariel, Umbriel, Titania, and Oberon—using spacecraft magnetometry measurements from flybys and orbiters. Amongst the 27 known Uranian moons, these are the only bodies sufficiently large to likely retain liquid water today. Furthermore, with the possible exception of that of Oberon, their surfaces show geomorphological evidence for resurfacing following accretion which may be a signature of past or present subsurface water. We consider the approach of magnetic induction whereby a spacecraft magnetometer senses magnetic fields from electrical currents in the oceans generated by Uranus's time-varying magnetic field. We focus on

Ariel in particular since it is the most likely amongst the major moons to have a present-day ocean and because it experiences some of the strongest variations in the Uranian field.

This work, first presented in meeting form (Weiss et al., 2021; Weiss et al., 2020), was conducted simultaneously and independently of two complementary studies (Arridge & Eggington, 2021; Cochrane et al., 2021). The former focuses more on the two outermost moons and incorporates the effects of magnetospheric currents (Arridge & Eggington, 2021), while the latter focuses more on statistical induction forward models and the possible effects of an ionosphere and current sheet (Cochrane et al., 2021). Our study uniquely considers the implications of recent compositional and thermal evolution models for Ariel, including the possibility of a conducting briny rocky core, for detection and characterization of its liquid interior.

2 Interior Structures of the Major Moons

2.1 Overview of the major moons

Uranus' major moons have radii ranging from 235.8 km (Miranda) to 788.9 km (Titania), with their sizes generally increasing outwards with semimajor axis (with a slight decrease from Titania to Oberon) (de Pater & Lissauer, 2015). Their orbits are near-circular (eccentricities 0.0011 to 0.0039) and largely confined to the equitorial plane of Uranus (inclinations 0.041 to 0.13°, except for Miranda which is 4.3°) with semimajor axes ranging from 5.1 (Miranda) to 22.8 (Oberon) Uranus radii (R_U) (JPL Solar System Dynamics, 2021). They are not currently in mutual mean motion resonances (Ćuk et al., 2020; Tittemore, 1990).

The moons have mass ratios of silicate to ice ranging from ~0.5 to ~0.7 for all but Miranda, which has 0.3 (Hussmann et al., 2015). Their surfaces are dominated by H_2O ice [possibly in the form of methane clathrates (Schenk, 1991)], while CO_2 has also been identified on Ariel, Umbriel and Titania (Grundy et al., 2006). With the possible exception of Oberon, their surfaces show resurfacing, variably manifested as possible diapiric coronae, grabens, and/or cryovolcanic flows (Schenk & Moore, 2020). In particular, Ariel's surface consists of lightly cratered plains with viscously relaxed craters. The plains are dissected by 2-4 km deep troughs with floors covered with possible cryovolcanic materials interpreted to be H_2O ice and/or NH_3-hydrates (Cartwright et al., 2020; Schenk, 1991). The ages of the moons surfaces may be as young as 0.1-0.4 billion years (Ga) for Ariel and Miranda (Zahnle et al., 2003).

Three main theories for the moons origin have been proposed. First, they may have accreted out of material that condensed in a circumuranian nebula (Szulágyi et al., 2018). However, it is uncertain if this is consistent with Uranus's 98° obliquity, which is thought to be the product of giant impacts near the end of Uranus' formation (Kegerreis et al., 2018; Morbidelli et al., 2012; Rogoszinski & Hamilton, 2021; Safronov, 1966). An alternative scenario is that the moons accreted subsequently out of the ejecta disk (Ida et al., 2020; Rogoszinski & Hamilton, 2021; Slattery et al., 1991). A third possibility is that the moons formed from tidal interactions between Uranus and rings created from the disruption of cometary material [e.g., Crida & Charnoz (2012)].

In the circumuranian nebula formation by model by Szulágyi et al. (2018), the moons formed sufficiently early that they likely contained live ^{26}Al that could have driven early volatile melting and internal differentiation. Formation from an ejecta disk would likely have occurred after the ^{26}Al heat source was exhausted and would have required tidally-driven heating for moon interiors to partially melt. Lastly, following accretion in a first generation of rings, the moons could have been tidally heated during a period of high eccentricity orbits (Charnoz et al., 2011). In the latter scenario, the moons would have formed mostly undifferentiated and undergone partial melting. Neveu and Rhoden (2019a) suggested such bodies could sustain long-lived convection of brines in a porous rocky core (25% porosity).

2.2 Possible interior oceans

The heat responsible for the resurfacing of the moons may have been supplied by the gravitational energy of formation, radiogenic elements, and possibly tidal forcing (Hussmann et al., 2015). The relatively old surfaces and non-zero eccentricity observed at each moon suggests these bodies are not subject to significant tidal heating at present. However, the moons may have previously passed through one or more low-order mean motion resonances that may have generated substantial heating (Chen et al., 2014; Ćuk et al., 2020; Tittemore, 1990). Hence, the preservation of a deep relict ocean is mainly determined by the modalities of heat transfer since the moons emerged from past resonances. Considering the strong temperature-dependence of ice's thermal conductivity, the moons would freeze in a few hundred Ma following a melting event in the absence of a long-term heat source [following Castillo-Rogez et al. (2019)]. Clathrate hydrates in the icy shell could significantly slow freezing of the hydrosphere (Castillo-Rogez et al., 2019; Kamata et al., 2019). The porous briny core model (Neveu & Rhoden, 2019a) may not allow for the presence of deep oceans in the moons except for Ariel [preliminary results by Neveu and Rhoden (2019b)], whereas a clathrate-rich shell could likely maintain relict oceans in all the moons but Miranda [see also Hussmann et al. (2006)].

Given these uncertainties for the major moons, we consider a broad range of interior models consisting of two and three layers with spherical symmetry (Figure 1). The three-layer model, which represents the case of a relict ocean, consists of an innermost nonconducting rocky core of radius r_c overlain by a ocean of thickness, h and uniform conductivity, σ, and capped with a nonconducting icy shell of thickness, d [e.g., Zimmer et al. (2000)]. The two-layer model, which represents the briny core case, consists of an innermost porous briny core of thickness, h, and uniform conductivity, σ, capped with a nonconducting ice shell of thickness, d. The outermost ice layer in both models has a radius equal to mean radius of each moon, r_m. Mathematically, the two-layer model is an end-member of the three-layer case for which $r_c = 0$. Because theory and observations indicate the Uranian moons at most should have tenuous atmospheres (surface pressure <20 nbar even around the largest moon, Titania), we have not included an additional outer conducting layer associated with a putative ionosphere (Widemann et al., 2009). Also, we have not included the contribution from a putative metallic core because its contribution to the induction signal is expected to be small [e.g., Zimmer et al. (2000)]. Analysis of these and other additional conductive layers should be the subject of future work.

For Ariel, we focus on two particular realizations of the relict ocean and briny core models that are motivated by the above considerations. For Ariel's relict ocean model, we consider a <30 km-thick conductive ocean underlying a 170-km thick non-conducting clathrate-rich shell. For Ariel's briny core model, we consider a solid hydrosphere overlying a briny porous rocky core (25% porosity). Both structures are consistent with Ariel's estimated ratio of rock to ice, which would indicate a total hydrosphere thickness of ~150-200 km for a differentiated body. The electrical conductivities of the conducting briny layers in these two cases are based on the fact that accreted volatiles such as CO_2, NH_3 could significantly contribute to ocean conductivity in the form of bi/carbonate ions and ammonium. An average cometary composition would lead to an electrical conductivity of ~2 S m^{-1} (0°C) prior to an increase of the salinity as a consequence of freezing. For a 30-km thick relict ocean, the hypersaline waters could have a conductivity of 15 S m^{-1} based on terrestrial analogs (Rebello et al., 2020) and correcting for the effect of temperature (Smith, 1962). These are likely minimum values because we are not considering the effects of pressure, which tends to increase electrical conductivity at the tens of MPa relevant to Ariel's residual ocean (Schmidt & Manning, 2017) and because <30 km oceans would have even more concentrated solute. In the case of a porous core, the electrical conductivity of the mixture computed with Archie's law is of the order of 1-3 S m^{-1} for 30% brine mixed with rock (with the range reflecting uncertainties in brine temperature). For this study, we assume the mean value 2 S m^{-1}.

3 Methodology

3.1 Overview of magnetic induction

We employ the classic technique of magnetic induction to search for conducting subsurface saltwater oceans (Zimmer et al., 2000). Time-varying fields inside a conducting body generate currents by Faraday's law of induction. These currents in turn generate a secondary magnetic field by Ampere's Law that can be sensed by a magnetometer.

These driving fields can be used to probe for subsurface oceans as part of two major stages of exploration. First, detection of induced fields from a small number of close (i.e., <~1 moon radius in altitude) flybys could identify the existence of an ocean by measuring the induction response at a single frequency. However, degeneracies between the ocean thickness, ice thickness, and ocean conductivity make it challenging to determine these parameters separately from single-frequency sounding. This is what the Galileo mission achieved for Europa (Zimmer et al., 2000). Second, repeated, long-term (e.g., lasting for tens of moon orbital periods or more) measurements at a given moon could enable multi-frequency sounding data that could enable separate determination of the ocean thickness, ice thickness, and ocean conductivity (Seufert et al., 2011). This is the goal of the Europa Clipper mission (Raymond et al., 2015).

In the following, we begin by calculating the driving field, the time-variable field of Uranus as viewed by each moon. We will then use this to calculate the induced field. The spacecraft will measure a superposition of the steady component of the Uranian field, the driving field, and the induction field. As a metric for the feasibility of using magnetic induction to search for subsurface oceans, we will compare these fields to the nominal sensitivity of a spacecraft magnetometry investigation. For a typical spacecraft fluxgate magnetometer and/or gradiometer on ≳2 m long boom, magnetic field accuracies of <1 nT have been commonly achievable (Anderson et al., 2007; Connerney et al., 2017; Glassmeier et al., 2010; Kivelson et al., 1992).

3.2 Driving field

Our goal is to calculate the magnetic field in the time and frequency domain of each moon. At the locations of the moons orbits, Uranus's magnetic field is well described by a dipole offset from Uranus' center by ~0.3 R_{U} along the spin axis toward the geographic north pole and tilted by 59° (note that a spherical harmonic expansion using a fixed origin also has power dominated by the dipole terms) (Connerney et al., 1987). The wobbling of the field due to Uranus' rotation (17.2 h period), combined with orbital motion due to the moon's nonzero eccentricities and inclinations (periods ranging from 33.6-323 h from Miranda out to Oberon), collectively produce time variable fields in the reference frames and locations of the moons.

We calculated the moon's motions using their orbital elements (JPL Solar System Dynamics, 2021) as well as using SPICE kernels (The Navigation and Ancillary Information Facility, 2021). Because we found that the frequencies of the signals with amplitudes > 1 nT (as well as the amplitudes of these signals) for both approaches were essentially indistinguishable given the accuracy of our discrete fast Fourier transform (FFT) implementation (see below), here we report results using the orbital elements. In the moon's reference frames, *x* points from the moon toward Uranus, *y* points opposite the direction of orbital motion, and *z* completes the right handed-triad (nearly along the spin axis of Uranus).

For the Uranian field, we used the internal hexadecapole AH_5 magnetic field model derived from Voyager 2 Magnetometer data and Ultraviolet Spectrometer observations of aurora (Herbert, 2009) (Figure S1) at at the epoch of the Voyager 2 flyby (1986). Given the estimated magnetopause distance of ~19R_{U}, all of the moons with the occasional exception of Oberon and Titania should spend essentially all of their time within the magnetosphere (Paty et al., 2020). Furthermore, the large angle between Uranus's spin and offset dipole axes means that the moons will spend relatively little time near the magnetic equator where field perturbations associated with a magnetospheric plasma sheet could mask the induction signals (Cochrane et al., 2021). Because we are focused on the innermost moons, we have neglected the effects of external diurnally and seasonally-driven magnetospheric currents on the driving field; these are likely mainly relevant for Titania and Oberon (Arridge & Eggington, 2021) and should be the subject of future work.

We calculated the field at each moon with a time interval of 0.01× the synodic frequency over aduration of 10^7× the synodic frequency. These were chosen to minimize spectral leakage and the picket fence effect (Girgis & Ham, 1980) in the FFTs in order to accurately estimate the amplitudes of the synodic frequencies and their harmonics. We found that The highest amplitude variation is in the *x*-component followed by the *y*-component, with both components having near-zero mean and ~90° offset in phase with respect to one another (Figure 2). The *z*-component variations are much weaker (ranging from 14% down to 3% of that of the *x*-component proceeding outward from Miranda to Oberon) and with non-zero mean (Figure 2).

We find that the dominant frequency at the major moons is that of the synodic (i.e., time required for a moon to return to the same longitude above Uranus's surface). The periods, T, and total amplitudes, A, of the synodic variations range from ~35 h and ~330 nT at Miranda to ~18 h and ~3.6 nT out at Oberon. These frequencies have skin depths of ~33-46 km and ~91-130 km for oceans with conductivities like that expected for the relict ocean and briny core scenarios, respectively. Furthermore, the moons experience a rich range of other driving frequencies at harmonics of the synodic frequency, their orbital frequencies, beating between the synodic and orbital frequencies, and harmonics of these frequencies (Figures 3, S3); similar results were obtained by Cochrane et al. (2021) and Arridge & Eggington (2021). We find that for Miranda, Ariel, and Umbriel, the first four, three and two harmonics of the synodic period, respectively have amplitudes exceeding the nominal 1 nT magnetometry sensitivity threshold. Meanwhile, for

Titania and Oberon, only the first harmonic of the synodic period exceeds this value. The orbital frequency for all the moons are below this threshold largely due to the moons' low inclinations.

3.3 Induced field

We calculate the induced field, B_{ind}, using the two and three-layer models (Figure 1) following classic techniques in electrodynamics (Jackson, 1999; Parkinson, 1983; Srivastava, 1966; Zimmer et al., 2000). Let us express Uranus's field, $\vec{B}_{\text{U}}$, as a sum of a time-independent term, $\vec{B}_0$ and a time-variable primary field $\vec{B}_{\text{pri}}$ that drives induction. The primary field can be expressed as the sum $j = 1{:}\,N$ frequency components with amplitude, $\vec{B}_j$, frequency, $\omega_j = 2\pi/T_j$, and phase, δ_j, and oriented in the direction of unit vector $\vec{b}_j$ so that

$$\vec{B}_{\text{U}} = \vec{B}_0 + \vec{B}_{\text{pri}} = \vec{B}_0 + \sum_{j=1}^{N} B_j\, e^{-i(\omega_j t - \delta_j)} \vec{b}_j \tag{1}$$

The primary field frequencies induce oscillating dipole moments $\vec{M}_j = -(4\pi/2\mu_0) A_j e^{i\varphi_j} B_j \vec{b}_j r_m^3$, with amplitudes, A_j and phase lags $+\pi + \varphi_j$ relative to that of the driving field $(\omega_j - \delta_j)$; here μ_0 is the permeability of free space. The induced field is given by

$$\begin{aligned} \vec{B}_{\text{ind}} &= \sum_{j=1}^{N} \frac{\mu_0}{4\pi} \frac{3(\vec{r}\cdot\vec{M}_j)\vec{r} - r^2 \vec{M}_j}{r^5} \\ &= -\sum_{j=1}^{N} A_j e^{-i(\omega_j t - \varphi_j - \delta_j)} B_{\text{pri}} \frac{3(\vec{r}\cdot\vec{b})\vec{r} - r^2\vec{b}}{2r^5} r_m^3 \end{aligned} \tag{2}$$

for radial position from the center of the moon, $\vec{r}$, and where

$$A_j e^{i\varphi_j} = \left(\frac{r_0}{r_m}\right)^3 \frac{R_j J_{5/2}[(r_m - d)k_j] - J_{-5/2}[(r_m - d)k_j]}{R_j J_{1/2}[(r_m - d)k_j] - J_{-1/2}[(r_m - d)k_j]} \tag{3}$$

with

$$R_j = \frac{[(r_m - d - h)k_j] k_j J_{-5/2}[(r_m - d - h)k_j]}{3J_{3/2}[(r_m - d - h)k_j] - [(r_m - d - h)k_j] k_j J_{1/2}[(r_m - d - h)k_j]} \tag{4}$$

Here, J_m are Bessel functions of the first kind and order m and $k_j = \sqrt{i\omega_j \mu_0 \sigma}$. For the three-layer sphere (i.e., $r_m - d - h > 0$), R_j is in general nonzero, whereas for the two-layer sphere (i.e., $r_m - d - h = 0$), $R_j = 0$.

The skin depth, the depth at which the primary field declines by a factor of $1/e$ for a semi-infinite conducting half space, is given by $s = \sqrt{2/\omega_j \mu_0 \sigma}$. The induction amplitude grows and the phase delay shrinks as the ocean gets thicker (i.e., h increases) and/or more conductive (σ increases). When the skin depth approaches the ocean thickness (i.e., $h \approx s$), the amplitude and phase dependence pass through a local minimum (i.e., decrease and then increase over a limited range of h and σ) (Hand & Chyba, 2007). Eventually, as these two parameters increase further, a saturated state is reached with $A_j = 1$ and $\varphi_j = 0$. For thin oceans (i.e., $h \ll r_m$), equations (3) and (4) reduce to

$$A_j \approx \frac{2r_m h}{3s^2} = \frac{\mu_0 r_m h \omega_j \sigma}{6} \quad (5)$$

Therefore, all other parameters being fixed, larger moons and higher frequency driving fields produce higher amplitude induced fields.

Forward modeling the induction field [equation (2)] consists of choosing values for h, σ, and d and computing A_j and φ_j using equations (3) and (4). The inverse problem of solving for the three parameters h, σ, and d from the two observations A_j and φ_j at a single frequency is clearly nonunique. This is illustrated by the fact that a thick, low conductivity ocean will produce a similar amplitude induction field as a thin, conductive ocean (Khurana et al., 2009; Seufert et al., 2011). Furthermore, a thick ice shell and thick ocean will have a similar amplitude induction field as that of a thin ice and thin ocean (although the phase lag for the latter will be greater). The nonuniqueness can be broken by sounding at multiple frequencies, provided that the ocean is near saturation (i.e., $h \approx s$) for at least one of the frequencies.

4. Results

Because most of the variation at the synodic frequency at each moon occurs in the *x*- and *y*-components, the induction poles for these frequencies lie within ± ~4° of of the equators of all moons but that of Miranda (for which it lies with ± ~6°). The induction poles sweep across the moons with the associated induced moments oscillating in magnitude at their respective frequencies. This means that spacecraft flybys with closest approaches near the equatorial regions of the moons and that sample a widely distributed range of phases will enable the most sensitive induction studies.

The amplitude of induced fields depend on σ, d, and h while the phase depends on σ, d. The response exhibits a degeneracy in which a given measured amplitude and phase are each consistent with a wide range of combinations of σ and h (Figure 4A). The amplitude grows and the phase lag approaches 0 with increasing h (as more fluid can participate in the induction process) and increasing σ (as a given ocean approaches saturation) (Figure 4B, C). Following equation (5), the minimum ocean conductivity and thickness required to generate a 1-nT amplitude induction field at the surface induction pole grows monotonically with the moons' distance from Uranus (and therefore with the amplitude of Uranus' field), with the exception that the order of Ariel and Miranda are reversed because of Ariel's 2.5× larger radius (Figure 4A).

We first consider the case of ocean detection. We see that for the estimated conductivities of a relict ocean and briny core, surface measurements could detect conducting layers with minimum thicknesses as low as ~0.3 and ~2 km (for Miranda) and ranging up to ~5 and ~50 km (for Oberon), respectively under a nominal 50-km thick ice shell (Figure 4A). By comparison, oceans <<1 km are detectable at Europa; this is much smaller than that of the Uranian moons mainly because of Europa's large radius (twice that of Titania) and because it experiences a large synodic amplitude approaching that of Miranda (Figure 4A). Furthermore, for a single flyby of Ariel within 200 km of it surface [e.g., that proposed for insertion of a flagship mission into orbit around Uranus (Hofstdater & Simon, 2017)], we find that induced fields for relict oceans of thickness of just a few km as well as from the briny core structure should have amplitudes detectable with a typical magnetometry investigation (Figure S4). Likewise, Cochrane et al. (2021) have shown that even in the presence of a model ionosphere, a relict ocean with just 2 S m^{-1} conductivity and thickness of <10 km could be detectable.

With respect to ocean characterization, we find that multi-frequency sounding is likely readily achievable at least at Miranda and Ariel. In particular, for Ariel, separate determination of ocean thickness, ice thickness and ocean conductivity may be possible for conductivities >~ 1 S m^{-1} and ocean thicknesses >~ 20 km (Figure 4B, C). More generally, this investigation could be enabled by multiple ($\gtrsim$ 10-20) flybys of each moon and/or dedicated moon orbiters or landers.

5 Conclusions

The five major moons of Uranus may harbor relict oceans and/or briny cores underneath their ice shells. The time-variable Uranian magnetospheric field of Uranus could produce substantial induced magnetic fields in the liquid layers of these moons, dominantly at the synodic frequency and its harmonics. For a nominal 50-km thick ice layer, relict oceans layers with conductivities of 15 S m^{-1} and thicknesses of <7 km could be detected on the major moons by a close flyby of a typical spacecraft magnetometry experiment. Multi-frequency sounding from flybys could in principle characterize the ocean thickness and conductivity for at least Miranda and Ariel. As such, searching for subsurface oceans on the major moons using magnetic induction should be a key science objective of a future mission to the Uranian system.

Data Availability Statement

The internal magnetic field coefficients of Herbert (2009) were used to model Uranus's driving field. No data were created for this research.

Acknowledgments

We thank Marc Neveu for helpful discussions. We thank the NASA Jet Propulsion Laboratory (consulting services agreement #1662407), the NASA Europa Clipper project (University of Michigan/JPL SUBK00011438), the MIT Undergraduate Research Opportunites Program and the MIT Department of Earth, Atmospheric and Planetary sciences for support. Part of this work was carried out at the Jet Propulsion Laboratory, California Institute of Technology, under a contract with the National Aeronautics and Space Administration (80NM0018D0004). B. P. W. and J. B.

B. conceived the project, B. P. W. supervised the project, and all authors conducted calculations were involved in writing the manuscript. The authors declare no competing interests.

References

Anderson, B. J., Acuña, M. H., Lohr, D. A., Scheifele, J., Raval, A., Korth, H., & Slavin, J. A. (2007). The magnetometer instrument on MESSENGER. *Space Sci. Rev., 131*, 417-450.

Arridge, C. S., & Eggington, J. W. B. (2021). Electromagnetic induction in the icy satellites of Uranus. *Icarus, 367*, 114562.

Balint, T. S., Atkinson, D., Babuscia, A., Baker, J., Bradford, C., Elder, C., et al. (2020). *Uranus System Exploration Under the New Frontiers Mission Class (A Novel Perspective)*. Retrieved from https://baas.aas.org/pub/2021n4i040/release/1?readingCollection=7272e5bb

Cartwright, R. J., Beddingfield, C. B., Nordheim, T. A., Roser, J., Grundy, W. M., Hand, K. P., et al. (2020). Evidence for ammonia-bearing species on the Uranian satellite Ariel supports recent geologic activity. *Astrophys. J. Lett., 898*, L22.

Castillo-Rogez, J., Hesse, M., Formisano, M., & Sizemore, H. G. (2019). Conditions for the preservations of brines inside Ceres. *Geophys. Res. Lett., 46*, 1963-1972.

Charnoz, S., Crida, A., Castillo-Rogez, J. C., Lainey, V., Dones, L., Karatekin, O., et al. (2011). Accretion of Saturn's mid-sized moons during the viscous spreading of young massive rings: Solving the paradox of silicate-poor rings versus silicate-rich moons. *Icarus, 216*, 535-550.

Chen, E. M. A., Nimmo, F., & Glatzmaier, G. (2014). Tidal heating in icy satellite oceans. *Icarus, 229*, 11-30.

Cochrane, C., Nordheim, T. A., Vance, S. D., Styczinkski, M., Soderlund, K. M., Elder, C. M., et al. (2021). In search of subsurface oceans within the moons of Uranus. *Lunar Planet Sci. Conf. LII*, abstract #1559.

Connerney, J. E. P., Acuña, M. H., & Ness, N. F. (1987). The magnetic field of Uranus. *J. Geophys. Res., 92*, 15329-15336.

Connerney, J. E. P., Benn, M., Bjarno, J. B., Denver, T., Espley, J., Jorgensen, J. L., et al. (2017). The Juno Magnetic Field Investigation. *Space Sci. Rev., 213*, 39-138.

Crida, A., & Charnoz, S. (2012). Formation of regular satellites from ancient massive rings in the solar system. *Science, 338*, 1196-1199.

Ćuk, M., El Moutamid, M., & Tiscareno, M. S. (2020). Dynamical history of the Uranian system. *Planet. Sci. J., 1*, 22.

de Pater, I., & Lissauer, J. J. (2015). *Planetary Sciences* (Updated Second ed.). Cambridge, UK: Cambridge University Press.

Elder, C. M., Nordheim, T. A., Patthoff, D. A., Leonard, E., Cartwright, R. J., Cochrane, C., et al. (2021). Uranus Magnetosphere and Moons Investigator. *Lunar Planet Sci. Conf. LII*, abstract #2289.

Girgis, A., & Ham, F. M. (1980). A quantitative study of pitfalls in the FFT. *IEEE Trans. Aerosp. Electron. Syst., AES-16*, 434-439.

Glassmeier, K. H., Auster, H. U., Heyner, D., Okrafka, K., Carr, C., Berghofer, G., et al. (2010). The fluxgate magnetometer of the BepiColombo Mercury Planetary Orbiter. *Planet. Space Sci., 58*, 287-299.

Grundy, W. M., Young, L. A., Spencer, J. R., Johnson, R. E., Young, E. F., & Buie, M. W. (2006). Distributions of H_2O and CO_2 ices on Ariel, Umbriel, Titania, and Oberon from IRTF/SpeX observations. *Icarus, 184*, 543-555.

Hand, K. P., & Chyba, C. F. (2007). Empirical constraints on the salinity of the europan ocean and implications for a thin ice shell. *Icarus, 189*, 424-438.

Herbert, F. (2009). Aurora and magnetic field of Uranus. *J. Geophys. Res., 114*, A11206.

Hofstdater, M., & Simon, A. (2017). *Ice Giants: Pre-Decadal Survey Mission Study Report*. Pasadena, CA: Jet Propulsion Laboratory, Report JPL D-100520.

Hussmann, H., Sohl, F., & Spohn, T. (2006). Subsurface oceans and deep interiors of medium-sized outer planet satellites and large trans-neptunian objects. *Icarus*, *185*, 258-273.

Hussmann, H., Sotin, C., & Lunine, J. I. (2015). Interiors and evolution of icy satellites. In G. Schubert (Ed.), *Treatise on Geophysics* (Second ed., pp. 605-635). Amsterdam.

Ida, S., Ueta, S., Sasaki, T., & Ishizawa, Y. (2020). Uranian satellite formation by evolution of a water vapour disk generated by a giant impact. *Nature Astron.*, *4*, 880-885.

Jackson, J. D. (1999). *Classical Electrodynamics* (3rd ed.). New York: Wiley.

JPL Solar System Dynamics. (2021). Retrieved from https://ssd.jpl.nasa.gov/?sat_elem

Kamata, S., Nimmo, F., Sekine, Y., Kuramoto, K., Noguchi, N., Kimura, J., & Tani, A. (2019). Pluto's ocean is capped and insulated by gas hydrates. *Nature Geosci.*, *12*, 407-410.

Kegerreis, J. A., Teodoro, L. F. A., Eke, V. R., Massey, R. J., Catling, D. C., Fryer, C. L., et al. (2018). Consequences of giant impacts on early Uranus for rotation, internal structure, debris, and atmospheric erosion. *Astrophys. J.*, *861*, 52.

Khurana, K. K., Kivelson, M. G., Hand, K. P., & Russell, C. T. (2009). Electromagnetic induction from Europa's ocean and the deep interior. In R. T. Pappalardo, W. B. McKinnon, & K. Khurana (Eds.), *Europa* (pp. 571-586). Tucson, AZ: University of Arizona Press.

Kivelson, M. G., Khurana, K. K., Means, J. D., Russell, C. T., & Snare, R. C. (1992). The Galileo magnetic field investigation. *Space Sci. Rev.*, *60*, 357-383.

Morbidelli, A., Tsiganis, K., Batygin, K., Crida, A., & Gomes, R. (2012). Explaining why the uranian satellites have equatorial prograde orbits despite the large planetary obliquity. *Icarus*, *219*, 737-740.

The Navigation and Ancillary Information Facility (2021). Retrieved from https://naif.jpl.nasa.gov/naif/spiceconcept.html

Neveu, M., & Rhoden, A. R. (2019a). Evolution of Saturn's mid-sized moons. *Nature Astron., 3*, 543-552.

Neveu, M., & Rhoden, A. R. (2019b). Origin and evolution of Saturn's mid-sized moons. *EPSC Abs.*, EPSC-DPS2019-2713.

Nimmo, F., & Pappalardo, R. T. (2016). Ocean worlds in the outer solar system. *J. Geophys. Res., 121*, 1378-1399.

Parkinson, W. D. (1983). *Introduction to Geomagnetism*. Edinburgh: Scottish Academic Press.

Paty, C., Arridge, C. S., Cohen, I. J., DiBraccio, G., Ebert, R. W., & Rymer, A. M. (2020). Ice giant magnetospheres. *Phil. Trans. R. Soc. London A, 378*, 20190480.

Raymond, C. A., Jia, X., Joy, S. P., Khurana, K. K., Murphy, N., Russell, C. T., et al. (2015). Interior Characterization of Europa using Magnetometry (ICEMAG): Probing the Europan ocean and exosphere. *Fall AGU Meeting*, abstract P13E-08.

Rebello, L. R. B., Siepman, T., & Drexler, S. (2020). Correlations between TDS and electrical conductivity for high-salinity formation brines characteristic of South Atlantic pre-salt basins. *Water SA, 46*, 602-609.

Rogoszinski, Z., & Hamilton, D. P. (2021). Tilting Uranus: Collisions versus spin–orbit resonance. *Planet. Sci. J., 2*, 78.

Safronov, V. S. (1966). Sizes of the largest bodies falling onto the planets during their formation. *Soviet Astron.*, *9*, 987-991.

Schenk, P. M. (1991). Fluid volcanism on Miranda and Ariel: Flow morphology and composition. *96*, 1887-1906.

Schenk, P. M., & Moore, J. M. (2020). Topography and geology of Uranian mid-sized icy satellites in comparison with Saturnian and Plutonian satellites. *Phil. Trans. R. Soc. London A, 378*, 20200102.

Schmidt, C., & Manning, C. (2017). Pressure-induced ion pairing in $MgSO_4$ solutions: Implications for the oceans of icy worlds. *Geochem. Persp. Lett., 3*, 66-74.

Seufert, M., Saur, J., & Neubauer, F. M. (2011). Multi-frequency electromagnetic sounding of the Galilean moons. *Icarus, 211*, 477-494.

Slattery, W. L., Benz, W., & Cameron, A. G. W. (1991). Giant impacts on a primitive Uranus. *Icarus*, *99*, 167-174.

Smith, S. H. (1962). Temperature correction in conductivity measurements. *Limnol. Oceanogr., 7*, 330-334.

Srivastava, S. P. (1966). Theory of the magnetotelluric method for a spherical conductor. *Geophys. J. R. Astr. Soc., 11*, 373-387.

Szulágyi, J., Cilibrasi, M., & Mayer, L. (2018). In situ formation of icy moons of Uranus and Neptune. *Astrophys. J. Lett., 868*, L13.

Tittemore, W. C. (1990). Tidal heating of Ariel. *Icarus, 87*, 110-139.

Weiss, B. P., Biersteker, J. B., Colicci, V., Couch, A., Petropoulos, A., & Balint, T. (2021). Searching for subsurface oceans on the moons of Uranus. *Lunar Planet Sci. Conf. LII*, abstract #2096.

Weiss, B. P., Colicci, V., & Biersteker, J. B. (2020). Searching for subsurface oceans on the moons of Uranus. *AGU Fall Meeting*, abstract #P074-007.

Widemann, T., Sicardy, B., Dusser, R., Martinez, C., Beisker, W., Bredner, E., et al. (2009). Titania's radius and an upper limit on its atmosphere from the September 8, 2001 stellar occultation. *Icarus, 199*, 458-476.

Zahnle, K., Schenk, P., Levison, H., & Dones, L. (2003). Cratering rates in the outer Solar System. *Icarus*, *163*, 263-289.

Zimmer, C., Khurana, K. K., & Kivelson, M. G. (2000). Subsurface oceans on Europa and Callisto: Constraints from Galileo magnetometer observations. *Icarus, 147*, 329-347.

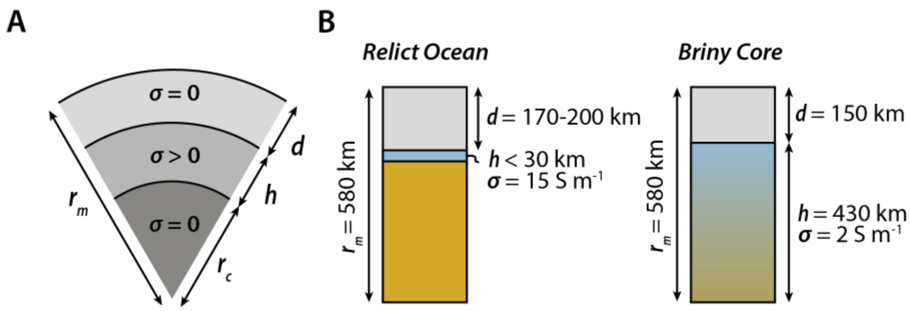

Figure 1. Assumed Moon interior models. (**A**) General model for all the moons, consisting of three-layer spherical body with a nonconducting rock ice core of radius r_c, overlain by a conducting layer of thickness, h, and conductivity, σ, which is in turn overlain by a nonconducting ice shell of thickness, d. (**B**) Two end-member spherically-layered models for Ariel. Left: relict ocean, consisting of <30 km-thick ocean with conductivity of up to 15 S m^{-1}. Right: briny core, consisting of 430 km-thick porous, rocky mantle with conductivity of 2 S m^{-1}.

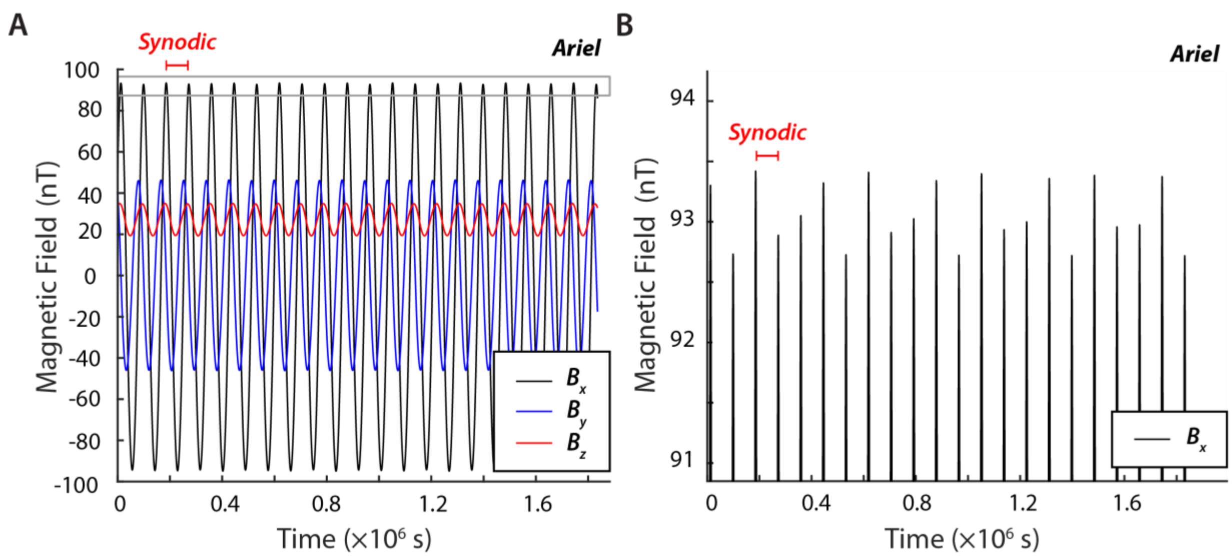

Figure 2. Uranus's time variable magnetic field as experienced by Ariel. (A) Three field components, where the *x* points toward Uranus, *y* points opposite the orbital velocity of the moon, and *z* completes the triad. The synodic period is labeled. (**B**) Zoom-in to grey boxed region in (A), showing the presence of additional frequencies modulating and interfering with the synodic frequency.

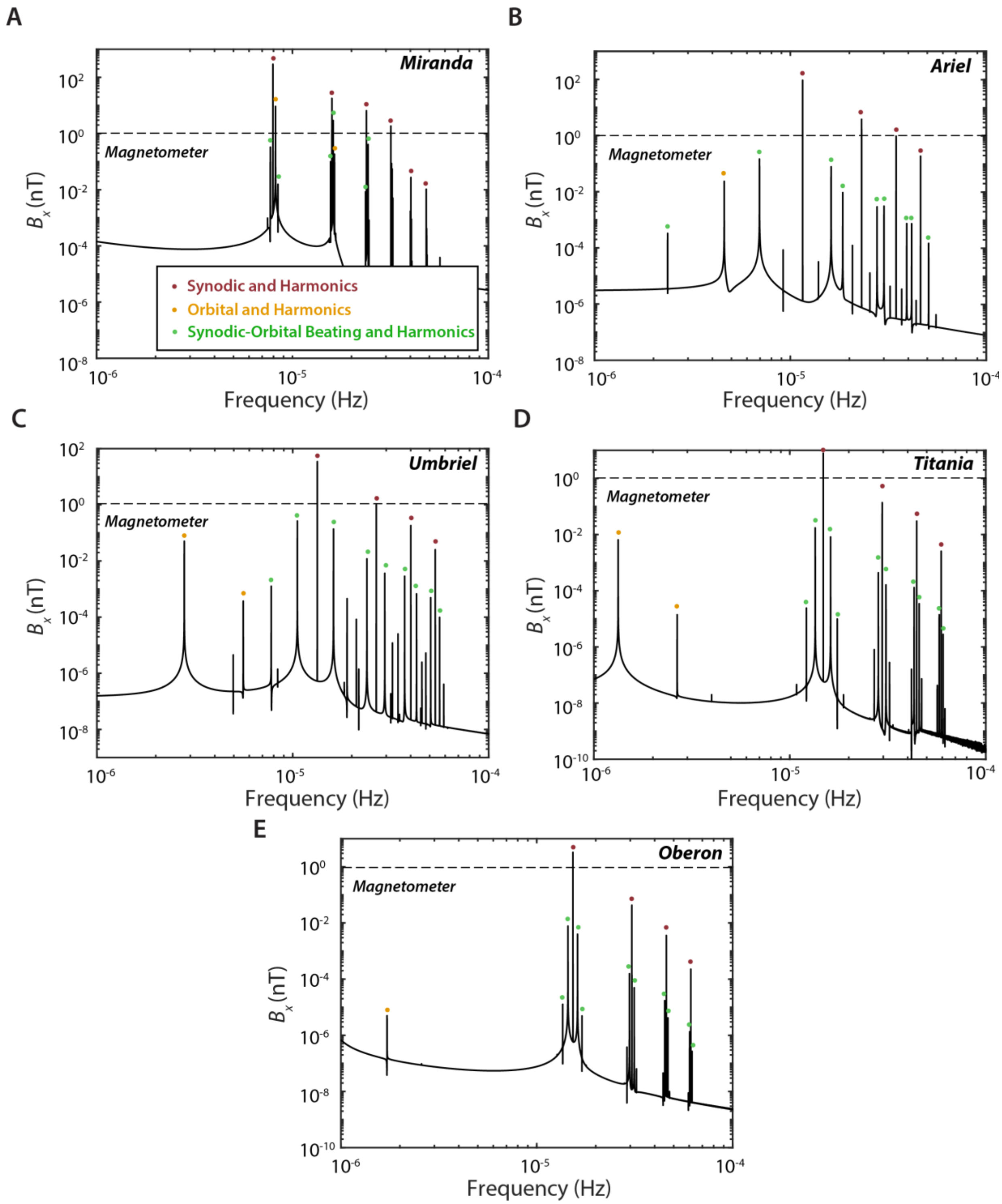

Figure 3. Periodogram of the *x*-component of Uranus's magnetic field as experienced by the major moons. There is a rich spectrum of frequencies including the synodic and its harmonics (red), the orbital frequency and its harmonics (orange), and beats between the synodic and orbital frequency

harmonics (green). Dashed lines denote 1 nT sensitivity of typical spacecraft magnetometry investigations. (**A**) Miranda. (**B**) Ariel. (**C**) Umbriel. (**D**) Titania. (**E**) Oberon.

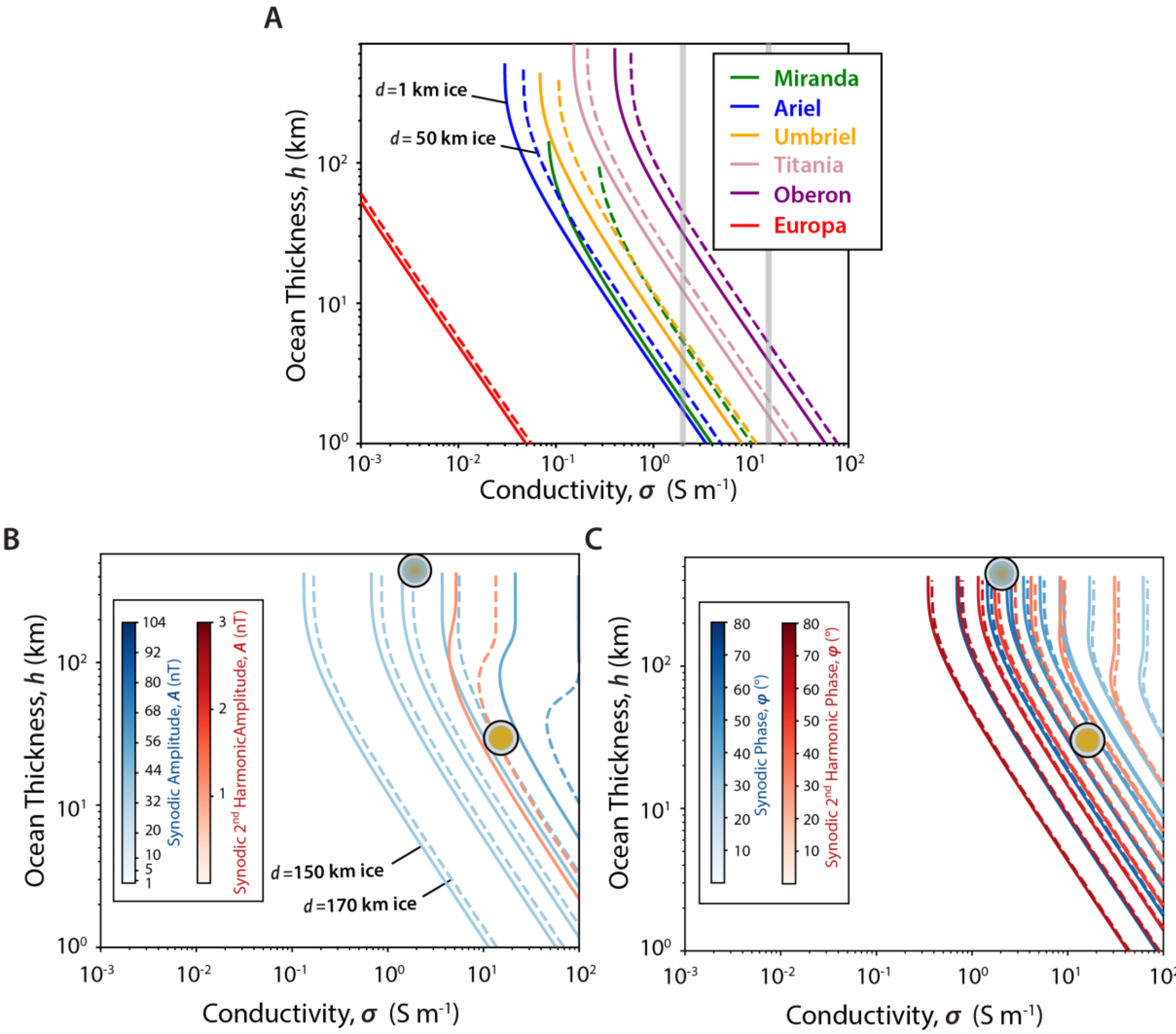

Figure 4. Induction fields at the synodic frequencies of the major moons and the Jovian moon Europa at the surface induction pole. (**A**) Combinations of ocean thickness and conductivity for producing a 1 nT amplitude. Solid and dashed curves are for ice thicknesses of 1 km (solid lines) and 50 km (dashed lines). Shown are conditions for Miranda (green), Ariel (blue), Umbriel (orange), Titania (pink), Oberon (purple), and Europa (red). Vertical grey bars denote conductivities for briny mantle (left) and relict (ocean). (**B, C**) Amplitude and phase of the response of the induced field for Ariel as function of ocean thickness and conductivity compared to two expected interior structures. Dashed curves denote end-member relict ocean, consisting of 30 km-thick ocean with conductivity of 15 S m^{-1}, overlain by a 170-km thick ice shell. Solid curves denote briny mantle, consisting of 430 km-thick porous, conducting mantle with conductivity of 2 S m^{-1} overlain by 150-km thick ice shell. Shown is the response to the first (red) and second (blue)

harmonics of the synodic frequency. Numerical values of contours correspond to labeled values on colorbars. Two colored circles denote briny ocean (top) (Fig. 1B) and 30-km thick relict ocean (bottom) (Fig. 1C). Note that electrical conductivities greater than 20 S m^{-1} are not expected even for hypersaline solutions due to interactions between ions and the low eutectic temperature of relevant solutions.

Supporting Information for:

Searching for Subsurface Oceans on the Moons of Uranus Using Magnetic Induction

Benjamin P. Weiss[1], John B. Biersteker[1], Vittorio Colicci[1], Allison Goode[1], Julie C. Castillo-Rogez[2], Anastassios E. Petropoulos[2], and S. Tibor Balint[2]

[1]Department of Earth, Atmospheric and Planetary Sciences, Massachusetts Institute of Technology, Cambridge MA, USA

[2]Jet Propulsion Laboratory, California Institute of Technology, Pasadena, CA, USA

Corresponding author: Benjamin Weiss (bpweiss@mit.edu)

Submitted to: *Geophysical Research Letters*

Contents of this file:

Figures S1 to S4

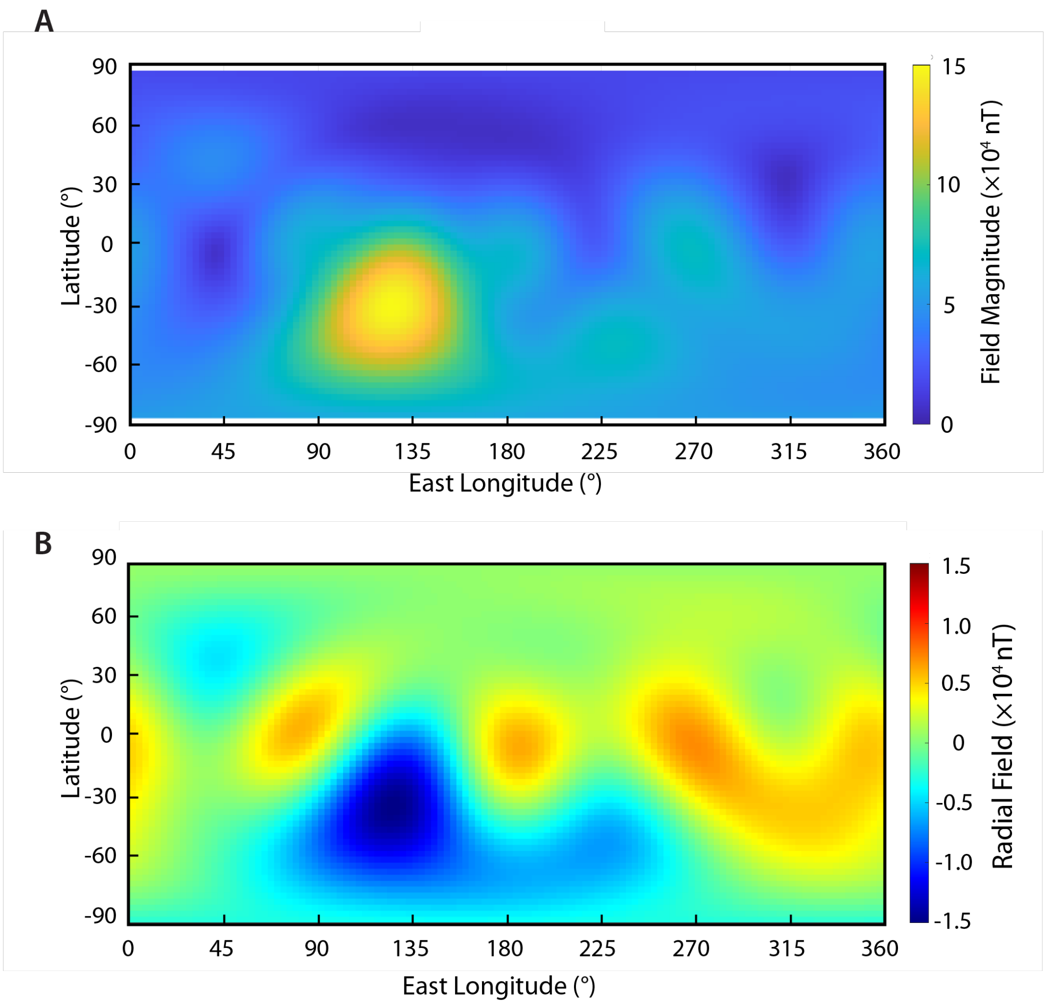

Figure S1. Uranus' magnetic field as measured by Voyager 2. Shown is the AH_5 hexadecapole model of Herbert (2009). (**A**) Field magnitude. (**B**) Radial field.

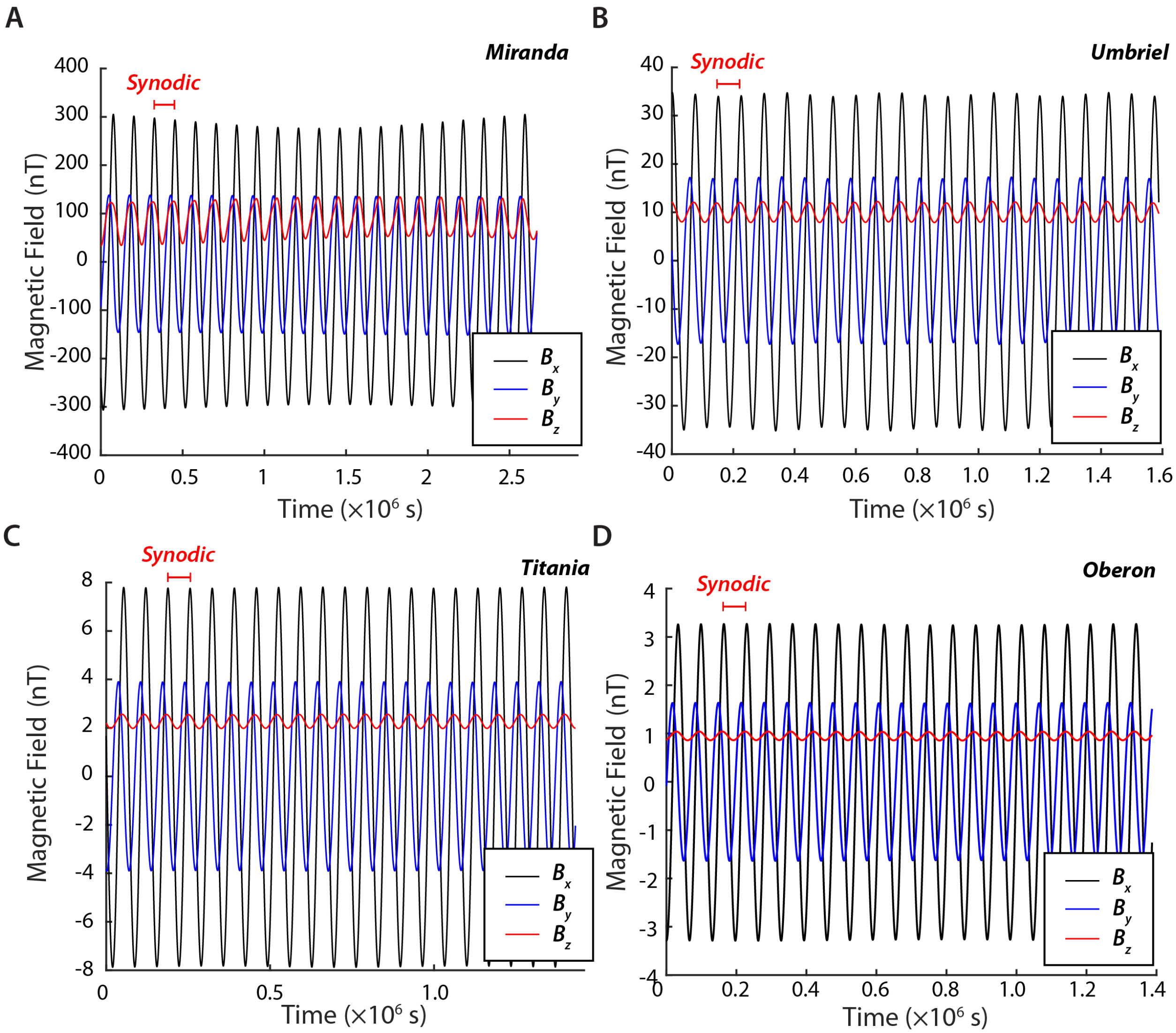

Figure S2. Uranus's time variable magnetic field as experienced by the other major moons. (A) Three field components, where the *x* points toward Uranus, *y* points opposite the orbital velocity of the moon, and *z* completes the triad. The synodic period is labeled. (**A**) Miranda. (**B**) Umbriel. (**C**) Titania. (**D**) Oberon.

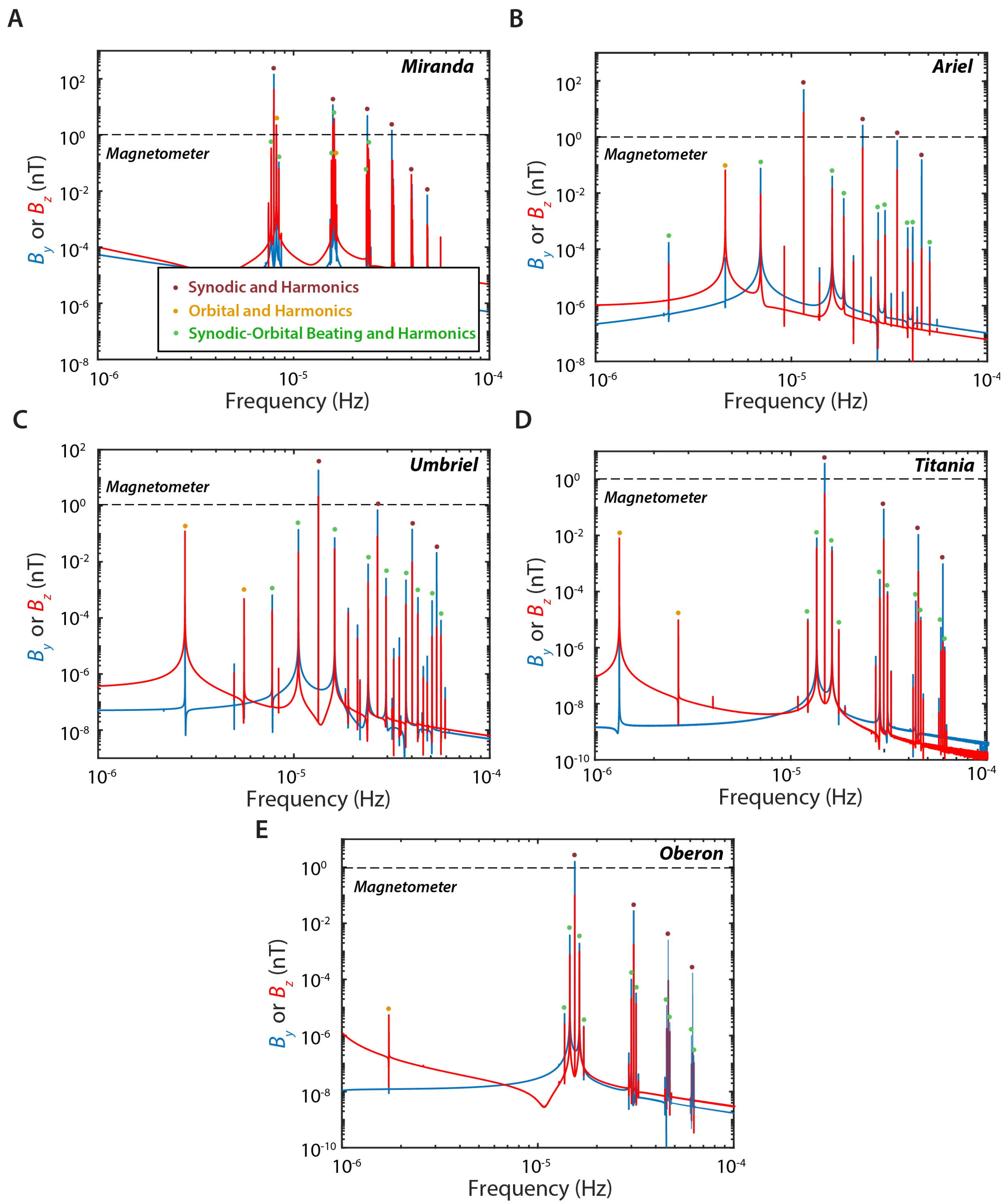

Figure S3. Periodograms of the *y*- and *z*-components of Uranus's magnetic field as experienced by the major moons. As with the *x*-components (Figure 3), there is a rich spectrum of frequencies including the synodic and its harmonics (red), the orbital frequency (orange), beats between the synodic and orbital frequency and harmonics of these beats (green). Dashed line denotes 1 nT sensitivity of typical spacecraft magnetometry investigations. Red boxes denote synodic frequencies and their harmonics. (**A, B**) *y*- (red) and *z*- (blue) components fo Miranda. (**C, D**) *y*-

(red) and z- (blue) components for Ariel. (**E, F**) y- (red) and z- (blue) components for Umbriel. (**G, H**) y- (red) and z- (blue) components for Titania. (**I, J**) y- (red) and z- (blue) components for Oberon.

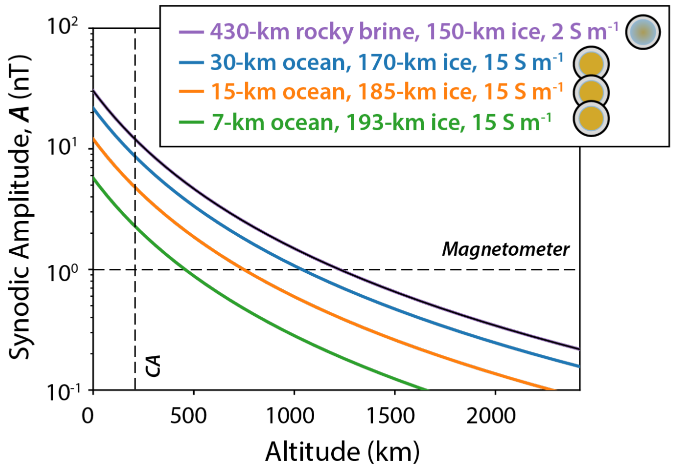

Figure S4. Amplitude of the induction signal at Ariel as a function of altitude above the surface induction pole. Shown is the response for four assumed interior structures. Purple curve denotes induced field for 430 km rocky brine with conductivity of 2 S m^{-1} overlain by 150-km thick ice layer. Blue, orange, and green curves denote induced fields for water oceans with conductivities of 15 S m^{-1} and fixed H_2O thickness of 200 km: 30-km ocean overlain by 170-km thick ice (blue), 15-km ocean overlain by 185-km thick ice (orange), and 7-km ocean overlain by 193-km thick ice (green). Horizontal and vertical dashed lines denote spacecraft magnetometry threshold and 200-km closest approach (CA) of an Ariel flyby from Hofstdater & Simon (2017).